

# Supplementary Information: Critical thermalization of a disordered dipolar spin system in diamond

Georg Kucsko,\* Soonwon Choi,\* Joonhee Choi,\* Peter C. Maurer, Hengyun Zhou, Renate Landig, Hitoshi Sumiya, Shinobu Onoda, Junichi Isoya, Fedor Jelezko, Eugene Demler, Norman Y. Yao, and Mikhail D. Lukin  
(Dated: January 27, 2018)

## CONTENTS

Materials and Methods	1
Sample Fabrication	1
Optical Setup	2
Microwave Setup	2
Magnetic Field Setup	2
Characterization of Experimental System	3
On-site Potential Disorder	3
Estimation of NV Density and Dipolar Interaction Strength	5
Inhomogeneity of the Microwave Field	7
Effective Hamiltonian of a Driven System	7
Resonance Counting Theory	10
Disorder-dependent Power-law Decay	10
Interplay between Dimensionality and long-range Interaction	11
Time-dependent Disorder	12
Detailed Analysis of Thermalization Experiments	13
Effective Disorder Control under Spin-locking Conditions	13
Effects of Incoherent Dynamics	14
Dependence of Thermalization Dynamics on Spin Bath Polarization	15
References	19

## MATERIALS AND METHODS

### Sample Fabrication

The diamond sample used in this work (type-Ib,  $\sim 4$  mm in diameter) was grown via high pressure and high temperature (HPHT), at 5.5 GPa and 1350 °C, using a Fe-Co alloy as a solvent. The main source of paramagnetic impurities was provided by substitutional nitrogen atoms in the neutral charge state (P1 centers) at a concentration of  $\sim 100$  ppm. A diamond plate of thickness  $\sim 1$  mm was obtained via laser cutting and polishing. To obtain NV centers, high energy electron irradiation was performed at  $\sim 2$  MeV with a flux of  $1.3\text{-}1.4 \cdot 10^{13} \text{ e} \cdot \text{cm}^{-2} \cdot \text{s}^{-1}$  and in-situ annealing at 700-800 °C up to a total fluence of  $1.4 \cdot 10^{19} \text{ cm}^{-2}$  (total time of 285 hrs). Additional annealing at 1000 °C for 2 hrs in vacuum was performed after half as well as after the full irradiation time. This process resulted in the diamond with NV centers of a concentration  $\sim 45$  ppm, corresponding to  $\sim 5$  nm of average separation and  $\sim (2\pi) 420$  kHz dipole-dipole interaction strength. To control the region of optical excitation, we used angle etching to create a beam-shaped piece of diamond, of 20  $\mu\text{m}$  length and  $\sim 300$  nm width, and transferred it onto our coplanar waveguide [1].

## Optical Setup

As shown in Fig. S1A, the optical setup consists of a home-built confocal microscope with a Nikon Plan Fluor 100x oil immersion objective ( $NA = 1.3$ ). The sample is mounted on a xyz-piezoelectric stage in the focal plane of the microscope. Excitation of the ensemble of NV centers is performed by illuminating a green laser ( $\lambda = 532$  nm) with average power less than  $50 \mu\text{W}$ . Short laser pulses are generated by an acousto-optic modulator (AOM) from Isomet in a double pass configuration. The  $\lambda/2$ -waveplate at the objective allows the control over the polarization of excitation light. NV centers emit fluorescence into the phonon sideband (630-800 nm), which is isolated from the excitation laser by a dichroic mirror. An additional 650 nm long-pass filter further suppresses the detection of unwanted signal. After passing a pinhole the collection beam is then focused onto a single photon counting avalanche photodiode (APD) to achieve detections with confocal resolution.

To probe the spin dynamics over time, we used a pulse sequence illustrated in Fig. S1B. We repeat the same pulse sequence twice, but include an extra  $\pi$ -pulse right before the read-out at end of the second sequence. The photon-count difference between the two read-outs allows us to measure the NV polarization, while being insensitive to changes in the background fluorescence due to charge dynamics [2].

## Microwave Setup

To coherently control the electronic spin states of NV centers we deliver microwaves to the sample through an impedance-matched coplanar waveguide fabricated on a glass coverslip. An omega-shaped microstructure (with a inner diameter  $20 \mu\text{m}$ ) at the center of the waveguide allows us to achieve Rabi frequencies up to  $\sim(2\pi) 100$  MHz. In Fig. S2, we illustrate the schematic diagram of the microwave control system. In order to have full control over two groups of NV centers with different transition frequencies, we employ two independent microwave circuits. In each circuit, a RF signal generator (Rohde & Schwarz SMIQ06B) produces the main driving frequency; an IQ mixer (Marki IQ1545LMP) generates pulsed signals; a low-pass microwave filter (Mini-Circuits VLF-3000+) suppresses unwanted higher-order harmonics of fundamental frequencies; and a DC block (Picosecond 5501a) additionally isolates the signals from low-frequency noises. After separately amplified (ZHL-16W-43+), two RF signals are then combined by a power combiner (Mini-Circuits ZFRSC-42-S+) and delivered to our sample. The inset of Fig. S2 depicts the detailed configuration of analog inputs (AI) connected to the IQ mixers. An arbitrary waveform generator (The Tektronix AWG7052) defines the duration and the phase of the pulses with a temporal resolution of 1 ns. For fine tuning of the voltage offset on the I and Q ports, a DC voltage is applied to the AWG signal. The addition of a 10-dB attenuator between the voltage source and the combiner suppresses unwanted reflections (see inset of Fig. S2).

## Magnetic Field Setup

For an external magnetic field, we use three water-cooled electromagnetic (EM) coils, which can provide a B-field up to  $\sim 300$  Gauss in an arbitrary orientation (see Fig. S1A and S3A).

As shown in Fig. S3B, we calibrate the magnetic field by recording electron spin resonance (ESR) spectra at various values of currents in the coils; since the Hamiltonian of a NV center in the presence of a magnetic field is known, the magnetic field at the position of our sample can be extracted from transitions frequencies of NV centers. For this process we utilize all four groups  $\{A, B, C, D\}$  of NV centers oriented in different crystallographic axes of diamond lattice, e.g.,  $A = [111]$ ,  $B = [\bar{1}\bar{1}1]$ ,  $C = [1\bar{1}\bar{1}]$ , and  $D = [\bar{1}1\bar{1}]$  (see Fig. S3C). Fig. S3D shows an ESR spectrum when the B-field is aligned along  $[111]$  direction; group A exhibits the largest Zeeman splitting, while the other groups B, C, and D become degenerate. In Fig. S3E, the direction of an external B-field is perpendicular to the sample surface, i.e.,  $B \parallel [001]$ , resulting in four degenerate groups.

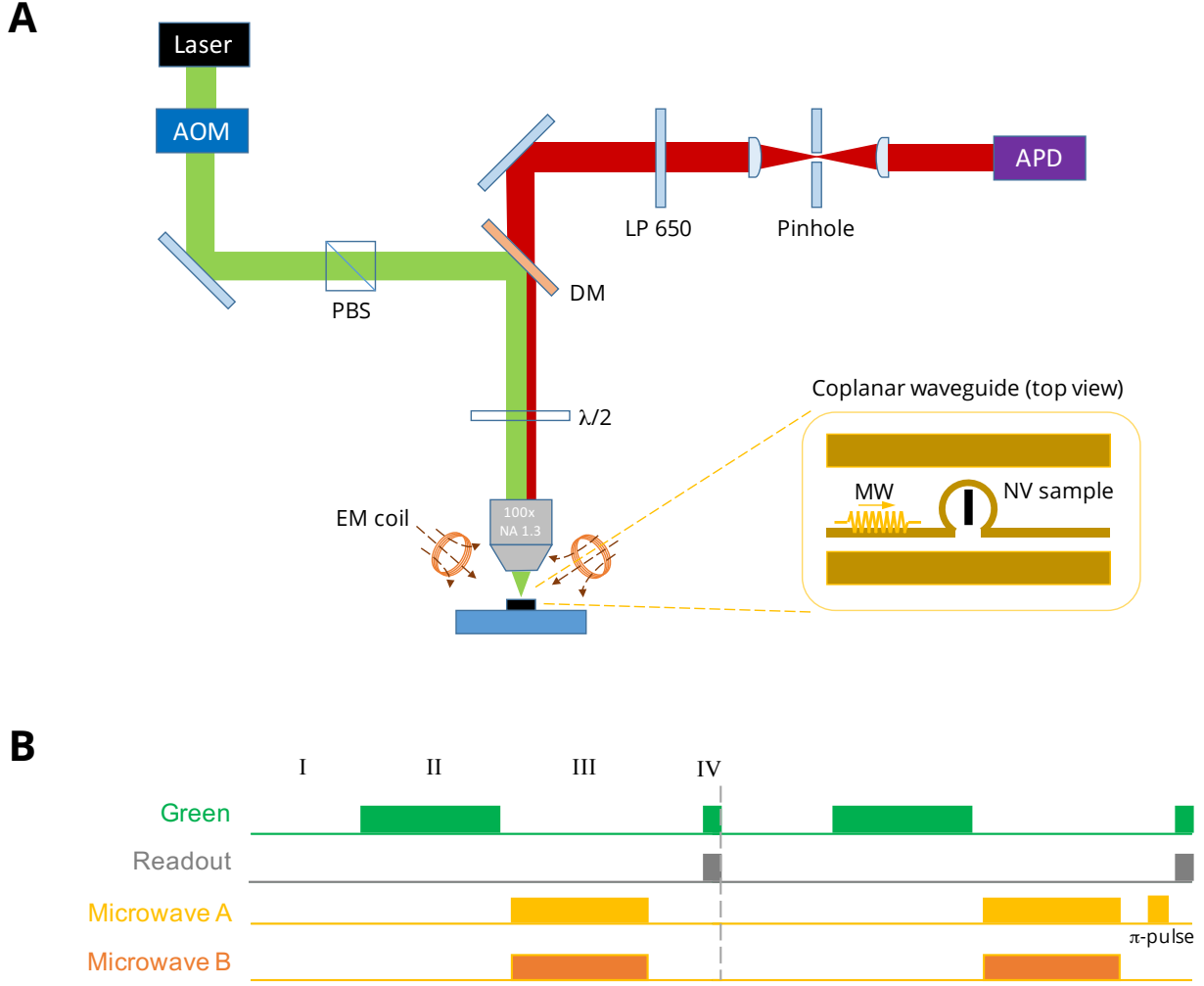


FIG. S1. **Schematic of the Optical Setup and the Pulse Sequence.** (A) Green and red lines indicate the optical paths (excitation: green, collection: red). An acousto-optic modulator (AOM) is used to control green laser duration. A dichroic mirror (DM) spectrally filters out the fluorescence from NV centers for electronic spin state readout. A 650 nm long pass filter additionally helps to filter fluorescence emission, corresponding to the phonon sideband (PSB) of NV centers. A 5- $\mu$ m pinhole is used in combination with a single photon counting avalanche photodiode (APD) to achieve confocal detection. A polarizing beam splitter (PBS) is used to polarize the excitation beam. With the addition of a  $\lambda/2$  waveplate we get control over the incident green polarization onto the diamond sample. The sample is placed ontop of a coplanar microwave (MW) structure in the shape of an omega (inset). Three electromagnetic coils are used to create a static magnetic field up to  $\sim 300$  Gauss in an arbitrary direction. (B) Typical experimental sequence used to measure NV dynamics. I: charge equilibration; II: spin polarization; III: experimental sequence; IV: spin readout.

## CHARACTERIZATION OF EXPERIMENTAL SYSTEM

### On-site Potential Disorder

The ESR linewidth of an NV ensembles is influenced by multiple factors. To discuss and estimate their contributions we introduce the ground state hamiltonian of the electronic spin state of a single NV center:

$$H = \left( \hbar \Delta_0 + d_{||} E_{||}^z \right) S_z^2 + \gamma_{NV} (\vec{S} \cdot \vec{B}) - d_{\perp} \left[ E_{\perp}^x (S_x S_y + S_y S_x) + E_{\perp}^y (S_x^2 - S_y^2) \right], \quad (\text{S1})$$

where  $S_x$ ,  $S_y$  and  $S_z$  denote the spin-1 matrices and  $\hbar$  the reduced Planck constant;  $\Delta_0 \approx (2\pi) 2.87$  GHz,  $\gamma_{NV} = (2\pi) 2.8$  MHz G $^{-1}$ ,  $d_{||} = (2\pi) 0.35$  Hz cm V $^{-1}$  and  $d_{\perp} = (2\pi) 17$  Hz cm V $^{-1}$  are the zero field splitting, the gyromagnetic

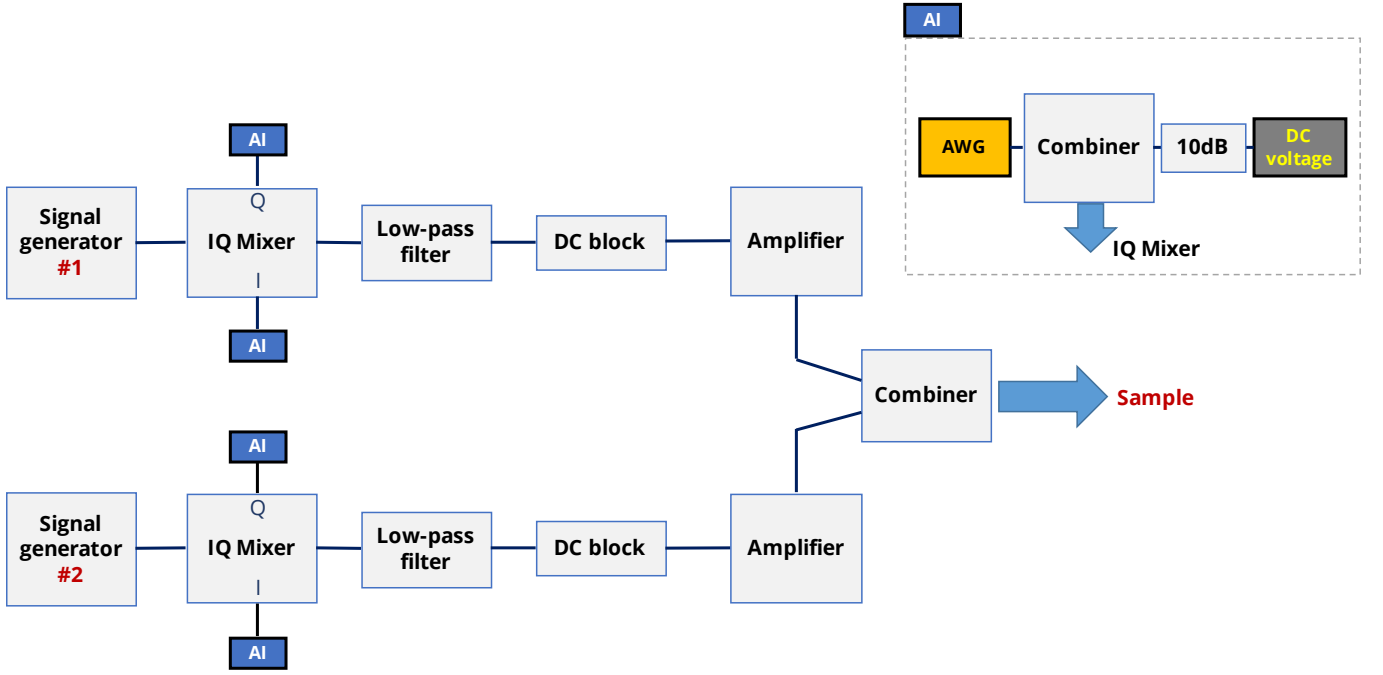


FIG. S2. **Schematic of the Microwave Control Setup.** Two sets of independent microwave circuits are used to achieve full control over two separate groups of NV centers at different transition frequencies. A 3 GHz low-pass filter suppresses unwanted higher-order harmonics. The two microwave paths are separately amplified to avoid saturation and then combined and sent to the diamond sample. In order to precisely control the microwave pulse length as well as phase, each path is sent through an IQ mixer controlled by an arbitrary waveform generator (AWG) output. The inset shows the detailed configuration of analog inputs connected to the IQ mixers used to define microwave pulse length and phase. In order to finely tune the voltage offset of the I and Q port, to achieve high isolation, a DC voltage source is combined with the AWG signal. The addition of an attenuator allows the suppression of unwanted reflections.

ratio, axial and perpendicular components of the ground triplet state permanent electric dipole moment of a NV center [3].  $B_{||(\perp)}$  and  $E_{||(\perp)}$  are projection of the effective magnetic and electric field parallel (perpendicular) to the NV axis. To a leading order, we ignore the effect of the perpendicular magnetic field noise  $\delta B_{\perp}$ , since it influence less on the spin coherence than the parallel one  $\delta B_{||}$ , owing to the large zero field splitting.

To account for effects of the local NV environment we include in  $B_{||}$  and  $E_{||(\perp)}$  on-site potential disorders originating from randomly distributed magnetic fields due to nuclear spins (i.e.  $^{13}\text{C}$  or  $^{14}\text{N}$ ) and paramagnetic impurities (i.e. P1 centers) as well as fields caused by local electric fields and lattice strain. To quantify the different contributions to the ESR linewidth, we conduct Ramsey spectroscopy in distinct basis states as listed in Fig. S4A. Since each basis has a well defined sensitivity to different physical noise sources, our Ramsey measurements provide insight into the local environment of the NV centers. Table SI lists the effects of magnetic and electric field noise on free induction decay of several different basis states. Figure S4 shows the outcome of Ramsey spectroscopy in the five different bases defined in SI.

Definition	Wavefunction	Precession rate	Noise	$1/T_2^*$
$ \psi_1\rangle$	$( 0\rangle +  1\rangle)/\sqrt{2}$	$\gamma_{NV} B_{  } + d_{  } E_{  }$	$\delta B_{  }, \delta E_{  }$	$\pi[\Gamma_{B_{  }} + \Gamma_{E_{  }}]$
$ \psi_2\rangle$	$( 0\rangle +  -1\rangle)/\sqrt{2}$	$\gamma_{NV} B_{  } + d_{  } E_{  }$	$\delta B_{  }, \delta E_{  }$	$\pi[\Gamma_{B_{  }} + \Gamma_{E_{  }}]$
$ \psi_3\rangle$	$( 1\rangle +  -1\rangle)/\sqrt{2}$	$2\gamma_{NV} B_{  }$	$\delta B_{  }$	$2\pi\Gamma_{B_{  }}$
$ \psi_4\rangle$	$( 0\rangle +  D\rangle)/\sqrt{2}$	$d_{  } E_{  } + d_{\perp} E_{\perp}$	$\delta E_{  }, \delta E_{\perp}$	$\pi[\Gamma_{E_{  }} + \Gamma_{E_{\perp}}]$
$ \psi_5\rangle$	$( 0\rangle +  B\rangle)/\sqrt{2}$	$d_{  } E_{  } + d_{\perp} E_{\perp}$	$\delta E_{  }, \delta E_{\perp}$	$\pi[\Gamma_{E_{  }} + \Gamma_{E_{\perp}}]$

TABLE SI. Five different basis states used for characterizing the local on-site disorder. The dark ( $|D\rangle \equiv (|1\rangle - |-1\rangle)/\sqrt{2}$ ) and bright states ( $|B\rangle \equiv (|1\rangle + |-1\rangle)/\sqrt{2}$ ) are prepared by applying an off-axis magnetic field perpendicular to an NV symmetry axis.  $\Gamma$  is a noise source-dependent inhomogeneous broadening contributing to the linewidth of the ESR.

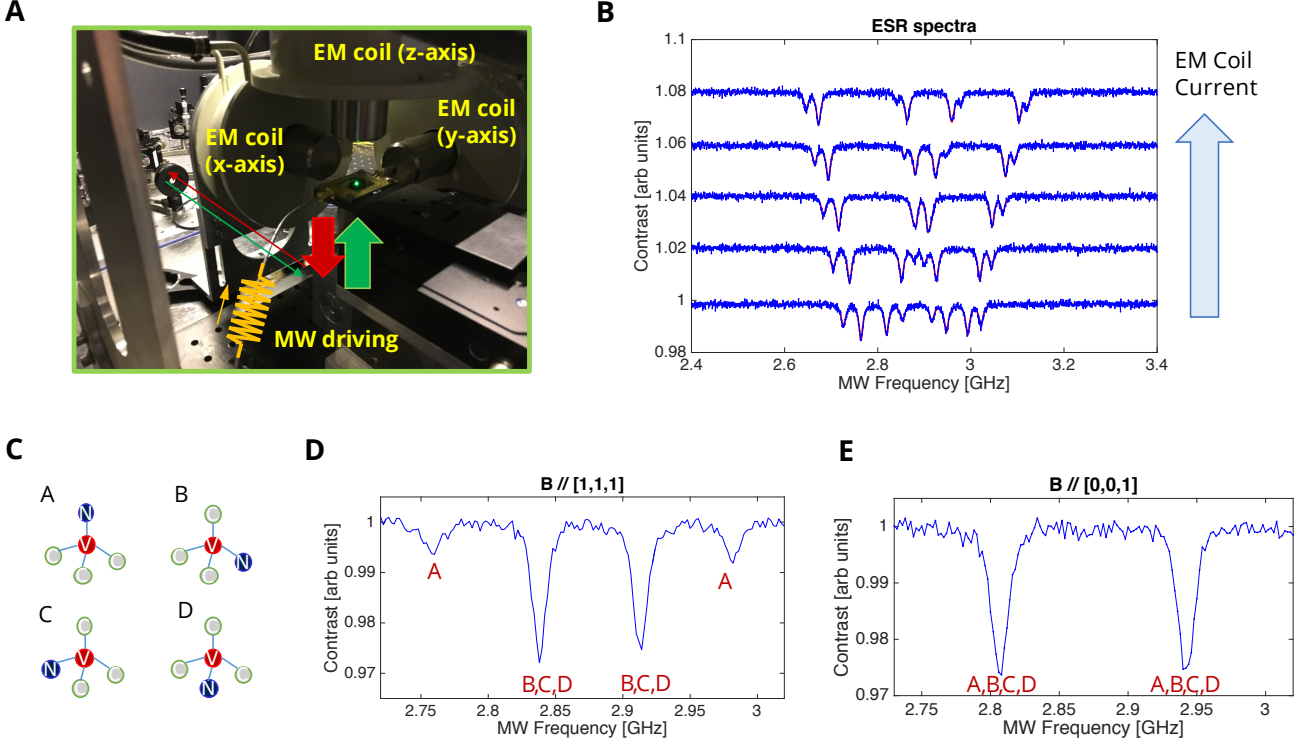


FIG. S3. **Magnetic Field Calibration and Control.** (A) Three electromagnetic (EM) coils are located in the vicinity of the diamond sample in order to provide an external magnetic field (B-field) in an arbitrary direction with an amplitude up to  $\sim 300$  Gauss. (B) To calibrate the coil's magnetic field, electron spin resonance (ESR) spectra are recorded for different values of coil currents. (C) The diamond lattice allows for four different crystallographic orientations of NV centers. The different groups A, B, C, and D of NV centers are characterized by their N-V axis orientations, i.e.,  $A = [111]$ ,  $B = [\bar{1}\bar{1}\bar{1}]$ ,  $C = [1\bar{1}\bar{1}]$ , and  $D = [\bar{1}\bar{1}1]$ . (D) Measured ESR spectrum for the B-field aligned along the  $[111]$  direction. Group A exhibits the largest Zeeman splitting (highest projected  $B_{||}$ ) because the spin quantization axis of group A is parallel to the chosen B-field. (E) Measured ESR spectrum for the B-field aligned along the  $[001]$  direction. Due to the  $[100]$  cutting direction of the diamond, all 4 NV groups form the same angle to the surface. With the external B-field being perpendicular to the sample surface, this leads to groups A-D having degenerate B field projections.

As seen in the table SI, each coherent superposition can effectively probe different types of noise components, enabling us to quantify the relative strengths of the on-site potential disorder. Using the identity  $\Gamma = 1/\pi T_2^*$  and the relations given in the last column of table SI, we can estimate a value for the different noise sources  $\Gamma_{B_{||}}$ ,  $\Gamma_{E_{||}}$ , and  $\Gamma_{E_{\perp}}$ . The discrepancy in  $T_2^*$  between  $|\psi_1\rangle$  and  $|\psi_2\rangle$  (as well as  $|\psi_4\rangle$  and  $|\psi_5\rangle$ ) in experimental data is presumably due to frequency-dependent field noise. By averaging these results, we can extract the three inhomogeneous broadening factors as  $\Gamma_{B_{||}} = 3.78(3)$  MHz,  $\Gamma_{E_{||}} = 2.18(8)$  MHz and  $\Gamma_{E_{\perp}} = 4.30(13)$  MHz. The measured ESR linewidth  $\Gamma_{\text{meas}} = \sqrt{8 \ln 2} W \approx 9.4$  MHz (see Fig. 1D, main text) roughly agrees up to a factor of  $\sim 1.5$  with the calculated  $\Gamma_{\text{calc}} \approx 6.0$  MHz. According to this analysis, the random on-site disorder in our sample seems to result from both electric and magnetic fields with comparable weights.

### Estimation of NV Density and Dipolar Interaction Strength

Due to the high density of NVs within our sample, the spin-echo coherence time is limited by interactions, as discussed in the main text. In particular, using the double electron-electron resonance (DEER) sequence presented in Fig. 2A in the main text, we verified experimentally that the additional dephasing of group A indeed originates from interactions with group B. Fig. S5 shows a measurement result of the DEER sequence in which we probe the relative spin-echo amplitude at a fixed time  $\tau$  as a function of driving frequency of group B. It shows a clear resonance when  $\omega = \omega_0^B$ , indicating that inter-group interactions between group A and B lead to enhanced dephasing.

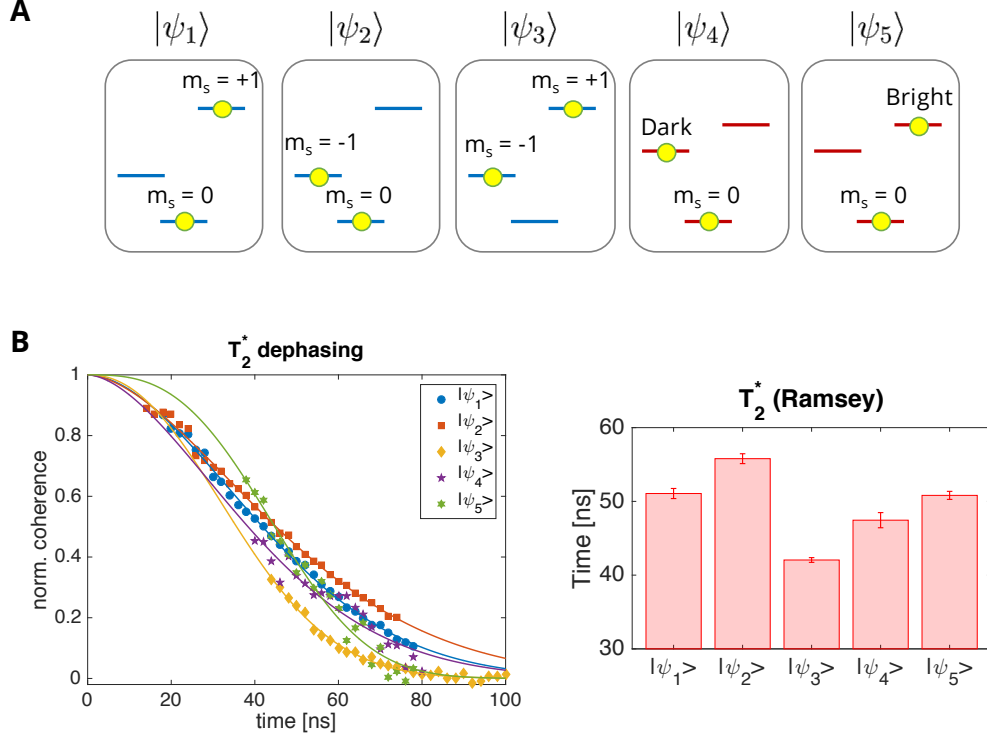


FIG. S4.  $T_2^*$  and  $T_2$  Measurements of different Basis States. **(A)** Different initial conditions used for coherence measurements. By aligning the magnetic field parallel (perpendicular) to the NV axis, the eigenbasis for the spin state of NV centers becomes  $\{|m_s = 0\rangle, |m_s = +1\rangle, |m_s = -1\rangle\}$  ( $\{|m_s = 0\rangle, |Dark\rangle, |Bright\rangle\}$ ), where Bright and Dark states are defined as even and odd combination of the original bare spin states  $|m_s = -1\rangle$  and  $|m_s = +1\rangle$ . **(B)** Ramsey spectroscopy data and extracted decay timescale for different initial states.

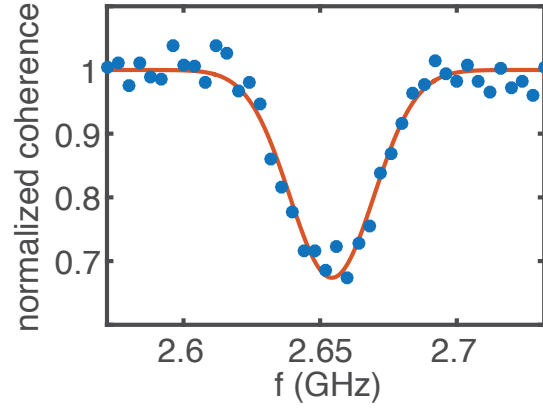


FIG. S5. **Intra-group Interaction Probed via Double Electron-Electron Resonance.** The relative, normalized spin echo coherence time at a fixed time  $\tau$  as a function of driving frequency of group B.

To quantitatively analyze the dependence of decoherence rate on the spin density, we study the dynamics of interacting spins using the exact diagonalization method with the effective Hamiltonian of Eq. (S24). Comparing the numerical result to the experimental data allows us to extract the density of NV spins in our sample.

Specifically, we simulate the time evolution of 12 NV spins under a spin echo pulse sequence protocol. The total NV concentrations selected for simulations are 5, 20, 40, 60, 70, 80 and 100 ppm. We averaged over  $\sim 500$  realizations of positional disorder, resulting in a single smooth coherence curve under the spin echo sequence. We fit the coherence decay with a simple exponential function and extract the decoherence rate,  $\gamma_T \equiv 1/T_2$ . Fig. S6A summarizes the

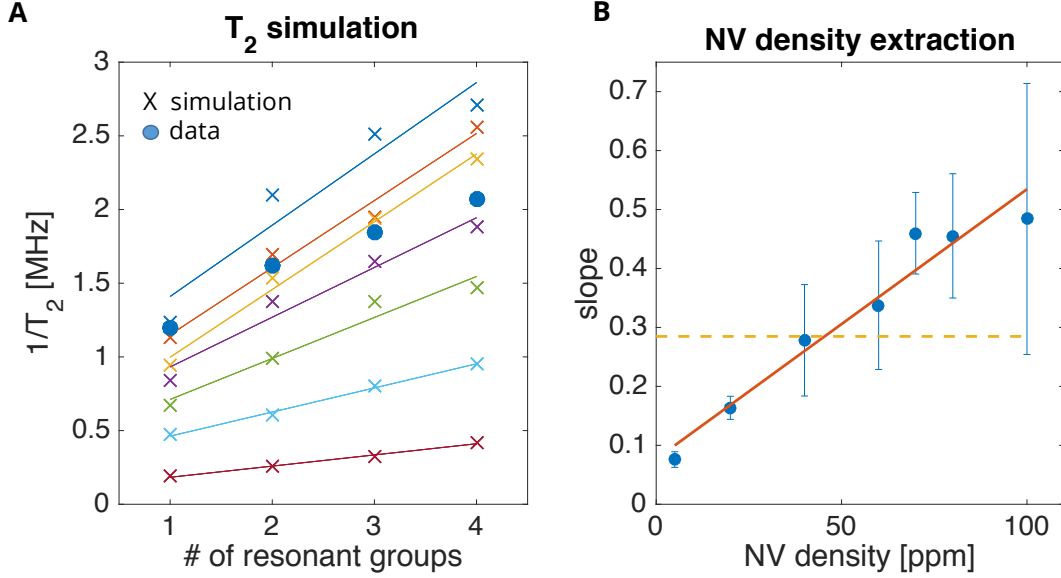


FIG. S6. **NV Density Extraction via Spin Echo Simulation.** (A) Comparison of the spin echo simulation results at different concentrations (crosses) to the measured data (circles). The total NV concentrations selected for the simulation are 5, 20, 40, 60, 70, 80 and 100 ppm. Solid lines are linear fits to the simulation to extract both  $\gamma_b$  and  $\gamma_0$  in the main text. (B) The NV concentration can be extracted by comparing the slopes ( $\gamma_0$ ) taken from the numerical simulations to the extracted slope of the experiment data (orange dashed line).

spin echo simulation results as a function of the number of resonant NV groups (effective density), where a linear dependence of  $\gamma_T$  is identified for all the density values. We model the decoherence rate as  $\gamma_T(\nu) = \gamma_b(\nu) + \nu\gamma_0(\nu)$ , where  $\nu$  is the number of resonant NV groups,  $\gamma_b$  and  $\gamma_0$  are density-dependent, bare and dipolar interaction-induced dephasing rates, respectively. Such linear dependence of  $\gamma_T$  on  $\nu$  is also confirmed in the experiment (see Fig. 2B in main text). By comparing  $\gamma_0$  between the experiment and the simulation, we estimate the NV density in our sample to be  $\sim 45$  ppm (see Fig. S6B).

### Inhomogeneity of the Microwave Field

Hartmann-Hahn resonances rely on the exact matching of Rabi frequencies of two driving fields  $\Omega_A = \Omega_B$ . Hence, stable and precise control of the driving strength is essential in our experiments. To this end, we estimate the inhomogeneity of our microwave driving field, by measuring the decay time of Rabi oscillations at various driving strengths (Fig. S7).

In an ideal case, the lifetime of Rabi oscillations generally increases due to suppression of disorder ( $T_2^*$ ). At higher driving strength ( $W_{\text{eff}} \sim \delta^I$ ) this lifetime should saturate due to the effect of Ising interaction. In our measurements however we observe a slight decrease in lifetime at high driving strengths, which is well explained by a 1.1% variation in Rabi frequency. We attribute this variation to spatial inhomogeneity in the driving field. With the strongest driving in our measurement  $\Omega = (2\pi) 32$  MHz, this effect leads to a spread in Rabi frequencies of  $\sim (2\pi) 0.3$  kHz. While it is still smaller than the effective disorder  $\sim (2\pi) 0.6$  kHz, such an inhomogeneity ultimately limits the maximum driving strength of our thermalization experiments.

### EFFECTIVE HAMILTONIAN OF A DRIVEN SYSTEM

In this section, we derive the effective Hamiltonian for a driven, dipolar interacting spin ensemble. The main idea is to work in a frame that is rotating along each NV group's quantization axis at corresponding driving frequency ( $\omega_0^A$  and  $\omega_0^B$  for group A and B, respectively). If the difference between  $\omega_0^A$  and  $\omega_0^B$  is large compared to the interaction strength, then one can ignore exchange interactions between spins from different groups (secular approximation). This

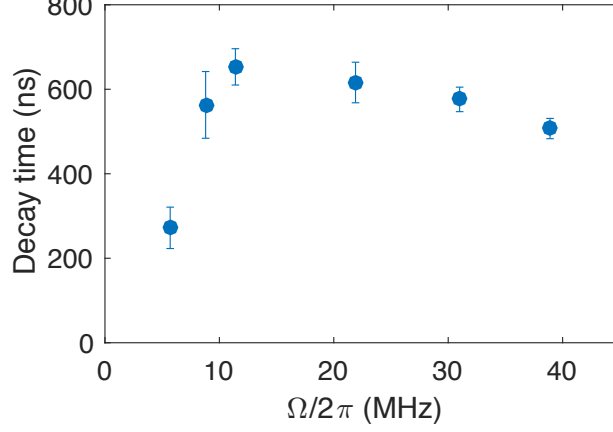


FIG. S7. **Rabi Oscillation Measurement.** Decay time of Rabi oscillations as a function of Rabi frequency  $\Omega$ .

results in distinct forms of intra- and inter-group interactions. We project the original Hamiltonian into two-level systems, and derive the effective Hamiltonian.

We start with the Hamiltonian for dipolar interacting NV centers

$$H = \sum_i H_i^0 + \sum_i H_i^d(t) + \sum_{ij} H_{ij}^{dd}, \quad (\text{S2})$$

where  $H_i^0$  is a single particle Hamiltonian for a spin at site  $i$ ,  $H_i^d(t)$  is time-dependent driving, and  $H_{ij}^{dd}$  is the magnetic dipole-dipole interaction between spins at sites  $i$  and  $j$ . The first term  $H_i^0$  includes Zeeman coupling to an external magnetic field, the zero field splitting of a NV center, and any other disordered potentials arising from couplings to paramagnetic impurities as described in the main text. In our experiments, dominant contributions for  $H_i^0$  come from the zero-field splitting  $\sim (2\pi) 2.87\text{GHz}$  and Zeeman field projected along the quantization axis (a few hundred MHz), which are two orders of magnitude larger than the rest of the couplings. Setting  $\hbar = 1$ , we can write

$$H_i^0 \approx (\Delta_0 + \delta_{0,i}) (\hat{c}_i \cdot \vec{S}_i)^2 + (\Delta_B(\hat{c}_i) + \delta_{B,i}) (\hat{c}_i \cdot \vec{S}_i) \quad (\text{S3})$$

where  $\vec{S}_i$  are spin-1 vector operators,  $\hat{c}_i$  is the unit vector along the quantization axis of the spin,  $\Delta_0 = (2\pi) 2.87\text{GHz}$  is the zero-field splitting,  $\Delta_B(\hat{c}_i)$  is the Zeeman splitting along  $\hat{c}_i$ , and  $\delta_{0,i}$  and  $\delta_{B,i}$  are on-site disorder potentials. If the external magnetic field  $\vec{B}$  is oriented in a way that  $\Delta_B(\hat{c}_i)$  for different groups are sufficiently separated (compared to the driving strength), one can effectively address distinct groups independently. Below we assume such a case and consider resonant driving of two groups  $A$  and  $B$  using microwave frequencies  $\omega_0^{A(B)} = \Delta_0 - \Delta_B(\hat{c}_{A(B)})$ . The Hamiltonian for such driving is given as  $H_i^d(t) = \gamma_{NV} \vec{B}_{MW} \cdot \vec{S}_i \cos(\omega_0 t)$ , where  $\gamma_{NV}$  is the gyromagnetic ratio of the NV center, and  $\vec{B}_{MW}$  is the microwave field vector. Now moving into the rotating frame with unitary transformation  $U(t) = \exp \left[ -i \left( \sum_i \Delta_0 (\hat{c}_i \cdot \vec{S}_i)^2 + \Delta_B(\hat{c}_i) (\hat{c}_i \cdot \vec{S}_i) \right) t \right]$  and applying rotating wave approximations, we obtain the effective single particle Hamiltonian

$$\bar{H}_i = U^\dagger(t) [H_i^0 + H_i^d(t)] U(t) - iU^\dagger \frac{d}{dt} U \quad (\text{S4})$$

$$= (\delta_{0,i} + \delta_{B,i}) |1\rangle \langle 1| + (\delta_{0,i} - \delta_{B,i}) |-1\rangle \langle -1| + \frac{\Omega}{2} (|-1\rangle \langle 0| + h.c.), \quad (\text{S5})$$

where  $\{|1\rangle, |0\rangle, |-1\rangle\}$  is the basis of spin states along its quantization axis and  $\Omega$  is the Rabi frequency of the driving.

The effective interaction among spins can be obtained in a similar way as follows. We start with the dipole-dipole interaction between spin- $i$  and spin- $j$

$$H_{ij}^{dd} = -\frac{J_0}{r^3} \left( 3 \left( \vec{S}_i \cdot \hat{r} \right) \left( \vec{S}_j \cdot \hat{r} \right) - \vec{S}_i \cdot \vec{S}_j \right), \quad (\text{S6})$$



where  $J_0 = (2\pi) 52 \text{ MHz} \cdot \text{nm}^3$  and  $\vec{r}$  is the relative position between two spins. In the rotating frame, we obtain the effective interaction by replacing  $\vec{S}_i \mapsto U^\dagger(t) \vec{S}_i U(t)$ . Since we are interested in the interaction in the basis of each NV's own quantization axis, we first explicitly rewrite  $\vec{S}_i$  in terms of  $(S_i^x, S_i^y, S_i^z)$  in a coordinate system where  $\hat{z}_i$  is parallel to the quantization axis  $\hat{c}_i$

$$\bar{H}_{ij}^{dd} = U^\dagger(t) H_{ij}^{dd} U(t) = -J_0/r^3 \left[ 3(\hat{r} \cdot \hat{x}_i)(\hat{r} \cdot \hat{x}_j) - \hat{x}_i \cdot \hat{x}_j \right] S_i^x S_j^x \quad (\text{S7})$$

$$+ 3(\hat{r} \cdot \hat{y}_i)(\hat{r} \cdot \hat{y}_j) - \hat{y}_i \cdot \hat{y}_j \Big] S_i^y S_j^y \quad (\text{S8})$$

$$+ 3(\hat{r} \cdot \hat{x}_i)(\hat{r} \cdot \hat{y}_j) - \hat{x}_i \cdot \hat{y}_j \Big] S_j^x S_j^y \quad (\text{S9})$$

$$+ 3(\hat{r} \cdot \hat{y}_i)(\hat{r} \cdot \hat{x}_j) - \hat{y}_i \cdot \hat{x}_j \Big] S_i^y S_j^x \quad (\text{S10})$$

$$+ 3(\hat{r} \cdot \hat{z}_i)(\hat{r} \cdot \hat{z}_j) - \hat{z}_i \cdot \hat{z}_j \Big] S_i^z S_j^z \quad (\text{S11})$$

$$+ H_{\text{rest}}, \quad (\text{S12})$$

where  $H_{\text{rest}}$  contains all the other terms of the form  $S^x S^z, S^y S^z, S^z S^x, S^z S^y$ .

We now perform rotating wave approximations. This is very well justified because the typical strength of the interaction is much weaker than the driving frequency  $J_0/r^3 \sim (2\pi) 0.4 \text{ MHz} \ll \omega_0^{A,B} \sim (2\pi) 2.5 \text{ GHz}$ . First, we note that  $S^x$  and  $S^y$  operators are rapidly oscillating in time while  $S^z$  remains invariant,  $[S_i^z, U(t)] = 0$ . Therefore, every term in  $H_{\text{rest}}$  may be safely ignored. Then, introducing

$$g_{ij}^+ = \frac{1}{2} \left[ 3(\hat{r} \cdot \hat{x}_i)(\hat{r} \cdot \hat{x}_j) - \hat{x}_i \cdot \hat{x}_j + 3(\hat{r} \cdot \hat{y}_i)(\hat{r} \cdot \hat{y}_j) - \hat{y}_i \cdot \hat{y}_j \right] \quad (\text{S13})$$

$$g_{ij}^- = \frac{1}{2} \left[ 3(\hat{r} \cdot \hat{x}_i)(\hat{r} \cdot \hat{x}_j) - \hat{x}_i \cdot \hat{x}_j - 3(\hat{r} \cdot \hat{y}_i)(\hat{r} \cdot \hat{y}_j) + \hat{y}_i \cdot \hat{y}_j \right] \quad (\text{S14})$$

$$h_{ij}^+ = \frac{1}{2} \left[ 3(\hat{r} \cdot \hat{x}_i)(\hat{r} \cdot \hat{y}_j) - \hat{x}_i \cdot \hat{y}_j + 3(\hat{r} \cdot \hat{y}_i)(\hat{r} \cdot \hat{x}_j) - \hat{y}_i \cdot \hat{x}_j \right] \quad (\text{S15})$$

$$h_{ij}^- = \frac{1}{2} \left[ 3(\hat{r} \cdot \hat{x}_i)(\hat{r} \cdot \hat{y}_j) - \hat{x}_i \cdot \hat{y}_j - 3(\hat{r} \cdot \hat{y}_i)(\hat{r} \cdot \hat{x}_j) + \hat{y}_i \cdot \hat{x}_j \right] \quad (\text{S16})$$

$$q_{ij} = 3(\hat{r} \cdot \hat{z}_i)(\hat{r} \cdot \hat{z}_j) - \hat{z}_i \cdot \hat{z}_j, \quad (\text{S17})$$

we can simply rewrite

$$\bar{H}_{ij}^{dd} \approx -J_0/r^3 \left[ g_{ij}^+ (S_i^x S_j^x + S_i^y S_j^y) + h_{ij}^- (S_i^x S_j^y - S_i^y S_j^x) + q_{ij} S_i^z S_j^z \right] \quad (\text{S18})$$

$$+ g_{ij}^- (S_i^x S_j^x - S_i^y S_j^y) + h_{ij}^+ (S_i^x S_j^y + S_i^y S_j^x) \Big]. \quad (\text{S19})$$

Here,  $g^+$  and  $h^-$  terms correspond to “flip-flop” type transitions, exchanging one unit of spin polarization,

$$(S_i^x S_j^x + S_i^y S_j^y) = |+\rangle\langle 0+| + |+-\rangle\langle 00| + |00\rangle\langle -+| + |0-\rangle\langle -0| + h.c. \quad (\text{S20})$$

$$(S_i^x S_j^y - S_i^y S_j^x) = i(|+\rangle\langle 0+| + |+-\rangle\langle 00| + |00\rangle\langle -+| + |0-\rangle\langle -0|) + h.c. \quad (\text{S21})$$

In addition, owing to the strong anharmonic level structure, we may also ignore flip-flop transitions between levels with large energy differences, e.g. terms such as  $|+-\rangle\langle 00|$ . Finally, we ignore the terms in Eq. (S19) as they correspond to double flip-up or flip-down and rapidly oscillate in time. After these approximations, the effective interaction becomes

$$\bar{H}_{ij}^{dd} \approx -J_0/r^3 \left[ (g_{ij}^+ + i h_{ij}^-) |+\rangle\langle 0+| + |0-\rangle\langle -0| + h.c. + q_{ij} S_i^z S_j^z \right]. \quad (\text{S22})$$

Now we divide into two cases depending on whether spins  $i$  and  $j$  belong to the same group or to different groups. In the former case, the quantization axes coincide, and we can simplify  $h_{ij}^- = 0$ ,  $g_{ij}^+ = \frac{1}{2}(1 - 3\cos^2\theta)$ , and  $q_{ij} = -(1 - 3\cos^2\theta)$  with  $\cos\theta \equiv \hat{z} \cdot \hat{r}$ . In the latter case, the flip-flop terms are again rapidly oscillating, and only the Ising interaction  $S_i^z S_j^z$  remains, resulting in

$$\bar{H}_{ij}^{dd} \approx \begin{cases} -\frac{J_0 q_{ij}}{r^3} \left( -\frac{|+\rangle\langle 0+| + |0-\rangle\langle -0| + h.c.}{2} + S_i^z S_j^z \right) & \text{same group} \\ -\frac{J_0 q_{ij}}{r^3} S_i^z S_j^z & \text{different groups} \end{cases}. \quad (\text{S23})$$

These interactions as well as the single particle terms conserve the total population of spins in  $|+\rangle$ . Therefore, once the system is initialized into a state with no population in  $|+\rangle$ , the dynamics remains in the manifold spanned by  $|-\rangle$

and  $|0\rangle$ . Projecting  $\sum_i \bar{H}_i + \sum_{ij} \bar{H}_{ij}^{dd}$  into this manifold, we obtain the Hamiltonian for an effective two-level system. Introducing spin-1/2 operators  $\vec{s}$  for two levels  $|-\rangle$  and  $|0\rangle$ , we obtain  $H_T = H_A + H_B + H_{AB}$ , where

$$H_{A(B)} = \sum_{i \in A(B)} [(\delta_{0,i} - \delta_{B,i}) s_i^z + \Omega_{A(B)} s_i^x] + \sum_{i,j \in A(B)} \frac{J_0 q_{ij}}{r_{ij}^3} (s_i^x s_j^x + s_i^y s_j^y - s_i^z s_j^z), \quad (\text{S24})$$

$$H_{AB} = - \sum_{i \in A, j \in B} \frac{J_0 q_{ij}}{r_{ij}^3} s_i^z s_j^z, \quad (\text{S25})$$

up to a constant.

Finally, we remark one particularly interesting aspect of this Hamiltonian in the dressed-state basis, i.e., quantization along  $s_i^x$ . With sufficiently strong driving,  $s_i^x$  becomes a good spin polarization basis, and one can rewrite the interactions in terms of  $s^\pm = s^y \pm i s^z$ , wherein the intra-group interaction becomes  $\propto s_i^x s_j^x + (s_i^+ s_j^+ + s_i^- s_j^-)/2$  and the inter-group interaction  $\propto (s_i^+ s_j^- + s_i^- s_j^+ + h.c.)$ . Here, we find that spin exchange terms  $(s_i^+ s_j^- + h.c.)$  are missing in the intra-group interaction. Omitting the energy non-conserving terms such as  $s_i^+ s_j^+$  (secular approximation with a strong driving strength  $\Omega$ ), we obtain the effective Hamiltonian described in the main text.

## RESONANCE COUNTING THEORY

In this section, we provide a detailed study of the single particle resonance counting theory. We will first focus on the case of quenched on-site potential disorder, deriving the disorder-dependent power-law relaxation presented in the main text. Then, we generalize the result to the case when disordered potentials are time-dependent.

### Disorder-dependent Power-law Decay

As discussed in the main text, we estimate the survival probability of a single spin excitation based on a simple counting argument. At time  $t$ , we compute the probability  $\text{Pr}(k; t)$  that the central spin is connected to  $k - 1$  other spins via a network of resonances, as defined in the main text. Assuming that the population of the excitation is equally shared among a resonating cluster, the survival probability is given as

$$P(t) \approx \sum_{k=1}^{\infty} \frac{1}{k} \text{Pr}(k; t). \quad (\text{S26})$$

reducing our problem to the computation of  $\text{Pr}(k; t)$ . Below we will show that the dominant contributions arise from  $k = 1$ , suggesting that finding a single resonant partner is usually enough to delocalize the spin excitation over the entire sample.

In general, the exact calculation of  $\text{Pr}(k; t)$  is difficult. This is because the connectivity of the resonance network is correlated due to the spatial structure ( $d$ -dimensional Euclidean space) as well as a given assignment of random on-site potentials, e.g., if spin pairs  $(a, b)$  and  $(b, c)$  are pair-wise resonant, it is likely that the pair  $(a, c)$  is also resonant, etc. However, the qualitative behavior of  $\text{Pr}(k; t)$  can still be well-understood by ignoring these correlations. In such a case, we may assume that the number of resonant partners  $\ell$  for a spins is drawn from a probability distribution  $p(\ell)$  and that this process can be iterated for each partner. We note that such a process may not terminate, in which case the central excitation becomes delocalized over a macroscopic number of spins. We first compute  $p(\ell)$  as a function of time  $t$ . For  $\ell = 0$ , a spin of interest (spin- $i$ ) must not have any resonating spins at any distance from  $r_{\min}$  to  $R(t) \equiv (J_0 t)^{1/3}$ , where  $r_{\min}$  is the short-distance cut-off. Hence,  $p(0; t)$  is given as a product of probabilities:

$$p(0; t) = \prod_{r_{\min} \leq r < R(t)} \left( 1 - 4\pi n r^2 dr \frac{\beta J_0 / r^3}{W_{\text{eff}}} \right) \quad (\text{S27})$$

$$= \exp \left[ - \int_{r_{\min}}^{R(t)} \frac{4\pi n Q_{\text{res}}}{r} dr \right] \quad (\text{S28})$$

where  $4\pi n r^2 dr$  is the probability of finding a spin at distance  $r$ , and  $Q_{\text{res}} = \beta J_0 / (W_{\text{eff}} r^3)$  is the probability that the spin resonates with the spin- $i$ . Defining  $\lambda(t) = 4\pi Q_{\text{res}} (\ln R(t) - \ln r_{\min})$ , we obtain  $p(0; t) = \exp[-\lambda(t)]$ . Similarly, we can calculate  $p(\ell; t)$  for  $\ell > 0$ , and obtain  $p(\ell; t) = \frac{1}{\ell!} (\lambda(t))^\ell e^{-\lambda(t)}$ , which is the Poisson distribution with mean  $\lambda(t)$ .

To show that the dominant contribution of Eq. (S26) arises from the  $k = 1$  term, we consider the probability of the termination of the resonance finding process,  $P_{\text{term}}$ . It satisfies the self-consistency equation

$$P_{\text{term}} = e^{-\lambda} + \sum_{\ell=1}^{\infty} \frac{\lambda^{\ell} e^{-\lambda}}{\ell!} (P_{\text{term}})^{\ell}, \quad (\text{S29})$$

where the first term corresponds to the case where the initial spin does not have any resonance up to time  $t$ , while the second term implies the termination of each sub-graph generated from  $\ell$  resonant spins. For sufficiently large  $\lambda$ ,  $P_{\text{term}}$  becomes small, and its contribution is dominated by the first term ( $\ell = 0$ ). In our case,  $\lambda(t)$  is a function of time which diverges in the limit  $t \rightarrow \infty$ . As we are interested in the late time dynamics, we may consider the first term only. In terms of  $\text{Pr}(k; t)$ , this corresponds to approximating  $\text{Pr}(k; t) \sim 0$  for  $k > 2$ . Finally, noting that that  $\text{Pr}(k = 1; t) = p(0; t)$ , we recover the expression in the main text.

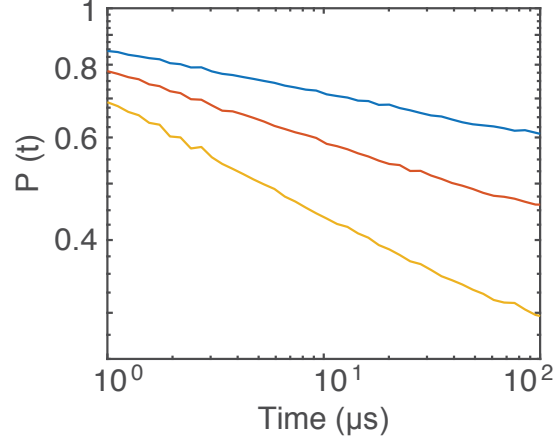


FIG. S8. **Single-particle simulation of power-law dynamics.** Blue, red, and yellow curve correspond to  $\Omega = (2\pi) 3, 8$ , and 20 MHz, respectively. For the simulations, we use  $10^4$  spins and average over more than  $10^3$  disorder realizations.

We numerically test the analytic resonance counting that predicts the power-law decay dynamics. In the limit of single-particle excitation, the survival probability  $P(t) = |\langle \psi(t) | \psi(0) \rangle|^2$  can be computed at any time  $t$  after the time evolution of a system under  $H_{\text{eff}}$  (See Eq. (1) in the main text). Considering physically relevant parameters used in the experiments, we verify such power-law decay dynamics for up to  $10^4$  spins as shown in Fig. S8. Moreover, we confirm the extracted power-law exponent is inversely proportional to effective disorder  $W_{\text{eff}}$  (Fig. 4C in the main text), further substantiating the thermalization mechanism based on rare resonances. The power-law exponents extracted from the simulations are summarized in Fig. S12A.

### Interplay between Dimensionality and long-range Interaction

The critical nature of a disordered dipolar spin ensemble in three dimensions originates from the interplay between long-range interactions and dimensionality. To see this, we can generalize the resonance counting analysis for a situation in which a single particle excitation is located in a  $d$ -dimensional spin system with long-range coupling decaying as  $1/r^{\alpha}$ . In such a setting, the survival probability  $P(t)$  can be expressed as,

$$P(t) = \exp \left[ - \int_{r_{\min}}^{R(t)} n S_d r^{d-1} \frac{\beta J_0 / r^{\alpha}}{W_{\text{eff}}} dr \right] \quad (\text{S30})$$

$$= \exp \left[ - \frac{n S_d \beta J_0}{W_{\text{eff}}} \int_{r_{\min}}^{R(t)} r^{d-\alpha-1} dr \right], \quad (\text{S31})$$

where  $S_d$  is the surface area of the  $d$ -dimensional volume. In fact, the argument of  $P(t)$ ,  $\int_{r_{\min}}^{R(t)} r^{d-\alpha-1} dr$ , is associated with the probability of finding a resonance up to the distance  $R(t)$  reachable at time  $t$ . Hence, when the dimensionality

$d$  is larger (smaller) than the interaction strength  $\alpha$ , the above integral diverges (converges) as  $R(t)$  becomes large, which implies delocalization (localization) of the single particle excitation. In the critical case where  $d$  is equal to  $\alpha$ , the resonance probability increases at a slow logarithmic rate, resulting in the power-law relaxation of the initial spin state as derived in Eq. (2) in the main text. In the limit of single particle excitations we therefore associate our system dynamics to such criticality behavior. However, due to the presence of many-spin excitations, much richer dynamics may appear at longer times. We attribute the deviation of power-law dynamics at late times observed in our experiments to this effect.

### Time-dependent Disorder

Now we consider the case of time-dependent disorder. For concreteness, we assume that the on-site potential disorder is given as a sum of a static and a dynamical disorder potential,  $\tilde{\delta}_i(t) = \tilde{\delta}_i^s + \tilde{\delta}_i^d(t)$ , where the static part  $\tilde{\delta}_i^s$  (dynamical part  $\tilde{\delta}_i^d(t)$ ) is random with zero mean and standard deviation  $W_s$  ( $W_d$ ). While  $\tilde{\delta}_i^s$  is time-independent, the dynamical component  $\tilde{\delta}_i^d(t)$  changes over time by uncorrelated jumps at a rate  $\Gamma = 1/\tau_d$ . Here, we focus on an experimentally relevant regime where  $W_s \gg W_d \gtrsim nJ_0 > 1/\tau_d$ .

As already mentioned in the main text, we modify the resonance criteria as follows. Two spins at sites  $i$  and  $j$  are on resonance at time  $t$  if: (1) *at any point in time*  $t' < t$ , their energy mismatch is smaller than their dipolar interaction strength,  $|\tilde{\delta}_i(t') - \tilde{\delta}_j(t')| < \beta J_{ij}/r_{ij}^3$ , and (2) the interaction occurs within the time-scale  $t$ ,  $J_{ij}/r_{ij}^3 > 1/t$ . While the second part of the condition is unchanged, the first part now captures that a pair may be brought into resonance by spectral jumps. Under the hierarchy of  $W_s \gg W_d \gtrsim nJ_0 > 1/\tau_d$ , the condition (1) can be approximated by two independent events: (a) the static energy mismatch is small enough,  $|\tilde{\delta}_i^s - \tilde{\delta}_j^s| < W_d$ , and (b) the dynamical energy mismatch is smaller than the coupling strength,  $|\tilde{\delta}_i^d(t') - \tilde{\delta}_j^d(t')| < \beta J_{ij}/r_{ij}^3$  at some time  $t' < t$ . In combination, the condition (1) is satisfied with the probability

$$P_{\text{res}}(r, t) \approx \frac{W_d}{W_s} \left( 1 - e^{-\frac{\beta J_0/r^3}{W_d} \frac{t}{\tau_d}} \left( 1 - \frac{\beta J_0/r^3}{W_d} \right) \right) \quad (\text{S32})$$

which is the product of probabilities for conditions (a) and (b). For the second factor, we used the probability that the initial configuration is off-resonant,  $(1 - \frac{\beta J_0/r^3}{W_d})$ , and the probability that none of the subsequent spectral jumps brings them into resonance  $e^{-\frac{\beta J_0/r^3}{W_d} \frac{t}{\tau_d}}$ . We note that, in practice, one should use  $\max(0, 1 - \beta J_0/W_d r^3)$  instead of  $(1 - \beta J_0/W_d r^3)$  since a probability cannot be less than zero. Finally, the survival probability is obtained by requiring no resonance at every distance  $r$  up to  $R(t) = (J_0 t)^{1/3}$

$$\overline{P(t)} = \exp \left[ - \int_{r=r_0}^{R(t)} 4\pi n r^2 P_{\text{res}}(r, t) dr \right], \quad (\text{S33})$$

where  $r_0$  is the short distance cut-off of the NV separations. We use the cut-off distance  $r_0 \sim 1.4$  nm, at which the corresponding dipole-dipole interaction is  $J_0/r_0^3 \sim (2\pi) 20$  MHz. Due to dipole blockade, a pair of NV centers closer than  $r_0$  cannot be addressed by microwave driving of Rabi frequency  $\Omega \sim (2\pi) 20$  MHz, which we use for initial preparations of spin states. Those spins do not participate in the spin exchange dynamics due to large energy mismatch. We note that,  $\lim_{\Gamma \rightarrow 0} P_{\text{res}}(r, t) \rightarrow Q_{\text{res}}(r) = \beta J_0/(W_s r^3)$  and the Eq. (S33) correctly reduces to the disorder-dependent power-law decay. In the presence of a small but finite  $\Gamma = 1/\tau_d$ , integrating Eq. (S33) using Eq. (S32) yields,

$$\overline{P(t)} = P_1(t) P_0(t), \quad (\text{S34})$$

where

$$P_1(t) = \exp \left[ - \frac{4\pi n}{3} \frac{W_d}{W_s} \left\{ J_0(t - t_0) - J_0(t e^{-\frac{\beta}{W_d \tau_d}} - t_0 e^{-\frac{t}{t_0} \frac{\beta}{W_d \tau_d}}) \right\} \right] \quad (\text{S35})$$

$$P_0(t) = \exp \left[ - \frac{4\pi n J_0 \beta}{3 W_s} \left\{ (1 + t/\tau_d) \mathcal{G}[0, \frac{\beta}{W_d \tau_d}] - (1 + t/\tau_d) \mathcal{G}[0, \frac{t}{t_0} \frac{\beta}{W_d \tau_d}] \right\} \right]. \quad (\text{S36})$$

Here  $\mathcal{G}$  is an incomplete Gamma function. In the limit of the hierarchy  $W_s \gg W_d \gtrsim nJ_0 > 1/\tau_d$ , we can simplify:

$$P_1(t) \approx C_1 \exp \left[ -\frac{4\pi n}{3} \frac{W_d}{W_s} \left( J_0 t (1 - e^{-\frac{\beta}{W_d \tau_d}}) \right) \right] \quad (\text{S37})$$

$$\approx C_1 \exp \left[ -\frac{4\pi n J_0 \beta}{3 W_s} \frac{t}{\tau_d} \right] \quad (\text{S38})$$

$$\equiv C_1 \exp[-t/T^*], \quad (\text{S39})$$

where  $C_1$  is a time-independent prefactor and

$$T^* = \frac{3W_s \tau_d}{4\pi n J_0 \beta} \propto \frac{W_s \tau_d}{n J_0}. \quad (\text{S40})$$

Similarly,  $P_0(t)$  can also be simplified as,

$$P_0(t) \approx C_2 \exp \left[ -\frac{4\pi n J_0 \beta}{3 W_s} \left\{ \mathcal{G}\left[0, \frac{\beta}{W_d \tau_d}\right] - \mathcal{G}\left[0, \frac{t}{t_0} \frac{\beta}{W_d \tau_d}\right] \right\} \right] \quad (\text{S41})$$

$$\approx C'_2 \exp \left[ -\frac{4\pi n J_0 \beta}{3 W_s} \ln(t/t_0) \right] \quad (\text{S42})$$

$$= C'_2 (t/t_0)^{-\frac{4\pi n J_0 \beta}{3 W_s}}. \quad (\text{S43})$$

Here we used the approximation  $\mathcal{G}(0, z) \approx -\ln(z) + \gamma + \mathcal{O}(z)$  for  $z \ll 1$ . Once again, we rediscover the power-law decay (Eq. (S43)) predicted in the main text, but now only up to a finite time  $T^*$ :

$$\overline{P(t)} = P_1(t)P_0(t) \propto e^{-t/T^*} t^{-\frac{4\pi n J_0 \beta}{3 W_s}}. \quad (\text{S44})$$

Therefore, according to the Eq. (S44), the weak time-dependent disorder results in a multiplicative exponential correction to the power-law decay up to  $t < T^*$ , beyond which the thermalization accelerates substantially. Furthermore, our theory model predicts that  $T^*$  is linearly proportional to the static disorder strength  $W_s$ , which is consistent with our observations (See Fig. 3D and Fig. 4D in the main text).

## DETAILED ANALYSIS OF THERMALIZATION EXPERIMENTS

### Effective Disorder Control under Spin-locking Conditions

To investigate the interplay between disorder and interaction experimentally, it is required to tune both disorder and interaction in a controlled way. In our experiments, we rely on a spin-locking technique in which both the energy spacing and the on-site disorder of a spin ensemble can be controlled in a continuous fashion.

As discussed in the main text, spin-locking allows us to prepare spins in the dressed state basis. In the new basis, the energy eigenstates are  $|\pm\rangle \approx (|m_s = 0\rangle \pm |m_s = -1\rangle)/\sqrt{2}$  and are split by an effective Rabi frequency of a spin-lock field,  $\Omega_{\text{eff}} = \sqrt{\Omega^2 + \delta^2}$ , where  $\Omega$  is the driving strength and  $\delta$  is the on-site disorder in the bare frame. Owing to a random distribution of  $\delta$ , the new level spacing  $\Omega_{\text{eff}}$  is also a random variable. Therefore, an effective disorder under the spin-locking condition can be defined as,

$$W_{\text{eff}} \equiv \sqrt{\text{Var}[\Omega_{\text{eff}}]} = \sqrt{E[\Omega^2 + \delta^2] - E[\sqrt{\Omega^2 + \delta^2}]^2}, \quad (\text{S45})$$

where  $\text{Var}[X]$  and  $E[X]$  are the variance and expectation value of a random variable  $X$ . Since the disorder in the bare frame follows a Gaussian distribution with a standard deviation  $W$ , the expectation values can be expressed as

$$E[\Omega^2 + \delta^2] = \frac{1}{\sqrt{2\pi}W^2} \int_{-\infty}^{+\infty} d\delta [\Omega^2 + \delta^2] e^{-\delta^2/2W^2} \quad (\text{S46})$$

$$E[\sqrt{\Omega^2 + \delta^2}] = \frac{1}{\sqrt{2\pi}W^2} \int_{-\infty}^{+\infty} d\delta \sqrt{\Omega^2 + \delta^2} e^{-\delta^2/2W^2}. \quad (\text{S47})$$

In the case of weak driving ( $\Omega \ll \delta$ ),  $W_{\text{eff}} \approx \sqrt{\text{Var}[\delta]} = W$ ; namely, the effective disorder is almost equal to that in the bare frame. However, as the driving strength  $\Omega$  increases we find  $W_{\text{eff}} \approx \sqrt{\text{Var}[\frac{\delta^2}{2\Omega}]} = \frac{W^2}{\sqrt{2\Omega}}$ . Hence, the effective disorder  $W_{\text{eff}}$  can be tuned by adjusting the Rabi frequency  $\Omega$  in the dressed state basis.

We note that the probability distribution of  $\Omega_{\text{eff}}$  is highly asymmetric, which may lead to small corrections to our counting argument at a quantitative level. To this end, for our numerical computations, we use an alternative definition of  $W_{\text{eff}}$  which is consistent with our resonance counting argument. Recall that two spins at site  $i$  and  $j$  with separation  $r$  are defined to be on resonance when  $|\tilde{\delta}_i - \tilde{\delta}_j| < \beta J_0/r^3$  and that we assumed this occurs with probability  $Q_{\text{res}} \propto (J_0/r^3)/W_{\text{eff}}$ . Therefore, the effective disorder strength  $W_{\text{eff}}$  should be defined in the same way from the full distribution of  $\Omega_{\text{eff}}$ . More specifically, we compute the probability  $q(\xi)$  that two independent random variables  $\tilde{\delta}_i$  and  $\tilde{\delta}_j$  satisfy  $|\tilde{\delta}_i - \tilde{\delta}_j| < \xi$  for a small parameter  $\xi$ . In the limit of  $\xi \ll W^2/\sqrt{2\Omega}$ , the probability  $q(\xi)$  is linearly proportional to  $\xi$ . Then, we define the effective disorder as  $W_{\text{eff}} \equiv \lim_{\xi \rightarrow 0} \xi/q(\xi)$ . Fig. S9 shows the dependence of  $W_{\text{eff}}$  as a function of  $\Omega$ . In the limit of large  $\Omega$ , the effective disorder scales as  $W_{\text{eff}} \propto 1/\Omega$ , as expected.

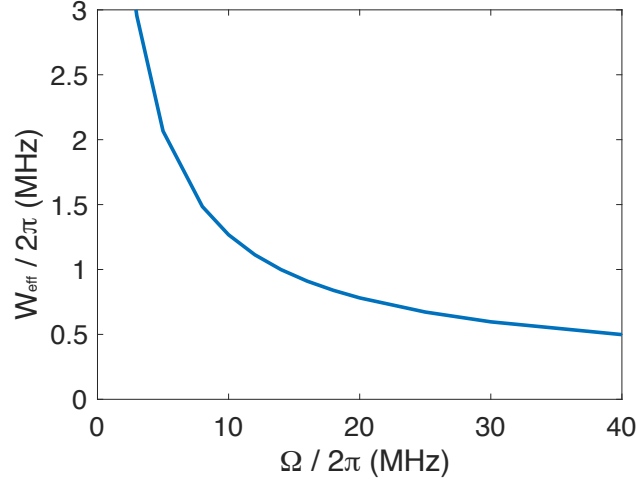


FIG. S9. **Effective disorder under spin locking conditions.** Based on the resonance counting argument, the effective disorder  $W_{\text{eff}}$  can be computed as a function of the Rabi frequency  $\Omega$ .

### Effects of Incoherent Dynamics

In our Hartmann-Hahn experiments, the spin dynamics are governed by both coherent cross-relaxation and incoherent depolarization. These two effects have qualitatively different dependence on the driving strength and can be clearly distinguished in our observations. To perform a detailed analysis of the results presented in the main text, we focus on the coherent dynamics by normalizing our data at the Hartmann-Hahn resonance  $\Omega_A = \Omega_B$  via a sufficiently detuned case  $|\Omega_A - \Omega_B| \gg nJ_0$ , at which the spin relaxations are dominated by incoherent dynamics (Fig. S10, blue line). Such normalization can be justified only if the two effects are independent and multiplicative. This is the case if the incoherent dynamics are induced by an independent Markovian noise, which results in an exponential and multiplicative factor  $e^{-\gamma t}$ . In our experiment, however, we observe a stretched exponential  $e^{-\sqrt{t/T}}$  decay profile from incoherent dynamics (Fig. 2D in the main text). Below, we explain why such incoherent decays are still factorizable.

Our incoherent dynamics can be modeled as follows. (See Ref. [2] for more details). Each spin at site  $i$  undergoes incoherent depolarization at rate  $\gamma_i$ . This rate  $\gamma_i$  is determined by the microscopic local environment of the spin and follows a random distribution  $\rho(\gamma; T_1^\rho)$ , such that the ensemble averaged polarization decays as a stretched exponential

$$e^{-\sqrt{t/T_1^\rho}} = \int_0^\infty \rho(\gamma; T_1^\rho) e^{-\gamma t} d\gamma. \quad (\text{S48})$$

The analytical expression as well as the microscopic origin of the distribution  $\rho(\gamma; T_1^\rho)$  are presented in Ref. [2]. At the Hartmann-Hahn condition, both the incoherent process and the coherent cross-relaxation lead to depolarization (see

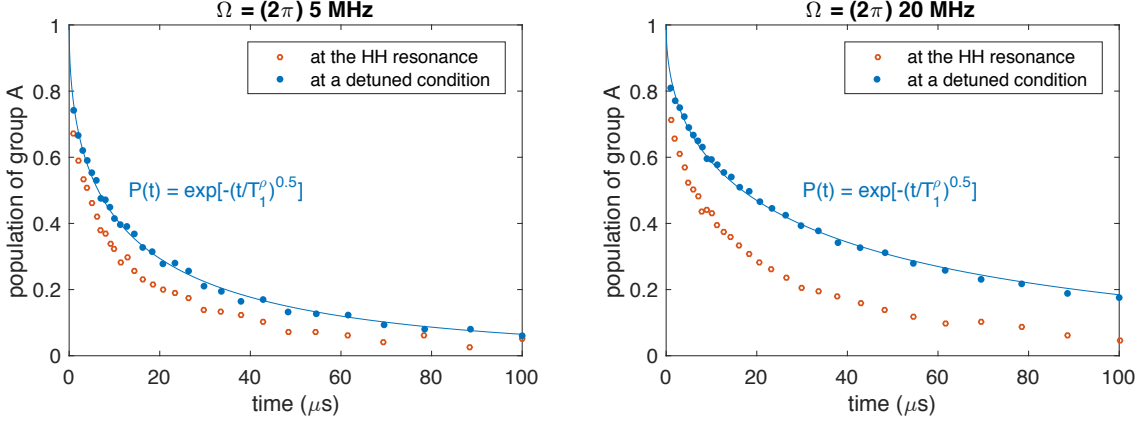


FIG. S10. **Unnormalized experimental Data.** Two data sets with different common Rabi frequencies of  $\Omega = (2\pi)$  [5, 20] MHz are presented at the Hartmann-Hahn resonance (red) and at the far-detuned case (blue). For the detuned signal, a stretched exponential of power 0.5 is fitted to the data.

Fig. S10). Hence, at time  $t$ , the rate of depolarization for spin- $i$  is given by  $\dot{p}_i(t) = -[\gamma_i + f_i(t)]p_i(t)$ , where  $f_i(t)$  is the rate of cross-relaxation (which generally depends on the state of other spins). This cross-relaxation, once averaged over an ensemble, leads to a power-law decay as derived in the previous section. The differential equation for the polarization is exactly solvable with the solution  $p_i(t) = e^{-\gamma_i t} e^{\int_0^t f_i(t') dt'}$ , where one finds a multiplicative exponential factor  $e^{-\gamma_i t}$ . Crucially, this effect is still factorizable, even after ensemble averaging:

$$\langle p_i(t) \rangle_{\text{ensemble}} = \int_0^\infty \rho(\gamma; T_1^\rho) e^{-\gamma_i t} d\gamma \left\langle e^{\int_0^t f_i(t') dt'} \right\rangle_{\text{ensemble}} \propto e^{-\sqrt{t/T_1^\rho}} \cdot t^{-\eta}, \quad (\text{S49})$$

where  $\eta$  is the disorder dependent exponent derived in the main text. Physically, this factorization arises because the microscopic environment for each spin, which determines coherent as well as incoherent dynamics, is random and independent. For this reason, in the experiment, we normalize the polarization decay at the Hartmann-Hahn resonance (Fig. S10, red line) by the incoherent decay at the far-detuned case (Fig. S10, blue line).

### Dependence of Thermalization Dynamics on Spin Bath Polarization

In Fig. S11, the theory prediction from Eq. (S33) is compared with experimental data for various Rabi frequencies and two different initial polarizations of group B spins. The functional profiles of the decay are consistent with power laws for over a decade, followed by accelerated, though still sub-diffusive relaxation at late times. In the power-law regime, we find that the power-law decay exponents depend on the initial polarization of group B spins (Fig. S12A). This is consistent with our theory; for single-particle dynamics, we expect that the power-law exponent scales as  $\sim nJ/W_{\text{eff}}$ , where  $n$  is the density of oppositely polarized spins. Indeed, when group B is initially unpolarized, the exponents are decreased by a factor of two compared to the fully polarized case, consistent with our theory at a quantitative level.

To characterize the late-time acceleration of the polarization decay, we use the time-dependent model where the pair-resonance counting criteria are modified as discussed in the previous section. By fitting the experimental data to our model using a Monte-Carlo (MC) optimization, we extract the parameters of the dynamical disorder strength  $W_d$  and spectral diffusion time  $\tau_d = 1/\Gamma$ . Here, we assume  $W_d$  as a global fit parameter which is independent from  $\Omega$ ; this is because we expect  $W_d$  to be predominantly determined by the mean-field interaction strength. In contrast,  $\tau_d$  may in principle be dependent on  $\Omega$  since the fluctuations of the Ising mean-field potential depend on the thermalization speed and hence also on the effective disorder strength tuned by  $\Omega$ . To this end, we performed two independent MC optimizations where we (i) treat  $W_d$  as global ( $\Omega$ -independent) and  $\tau_d$  as local ( $\Omega$ -dependent) variables (Fig. S11A), or instead (ii) fix both parameters as global variables (Fig. S11B). For the static effective disorder, we use the theory-predicted values  $W_s \sim W^2/\Omega$  (as described previously). Naturally, owing to the larger number of fit parameters, a global  $W_d$  with local  $\tau_d$  variation (Fig. S11A) shows better agreement than a global  $W_d$  together with global  $\tau_d$  (Fig. S11B). In the latter case, extracted fit parameters  $W_d$  and  $\tau_d$  are  $(2\pi) 46 \pm 14$  kHz and  $43 \pm 9$   $\mu\text{s}$ , respectively.

In the former case (Fig. S11A), the extracted dynamical disorder  $W_d \sim (2\pi) 0.5$  MHz is consistent with the expected strength of the Ising interaction, suggesting that spin-spin interactions play an important role for the time-dependent disorder. Furthermore,  $\tau_d$  is also consistent with the observed NV depolarization timescale, including contributions from both coherent cross-relaxation and incoherent spin depolarization. We note that in the fully polarized case the extracted values for  $\tau_d$  are smaller than those in the unpolarized case (Fig. S12B). We speculate that this could be due to faster coherent spin-exchange dynamics in the former case, giving rise to a faster fluctuation in  $\delta^I$ , responsible for the accelerated thermalization dynamics at late times.



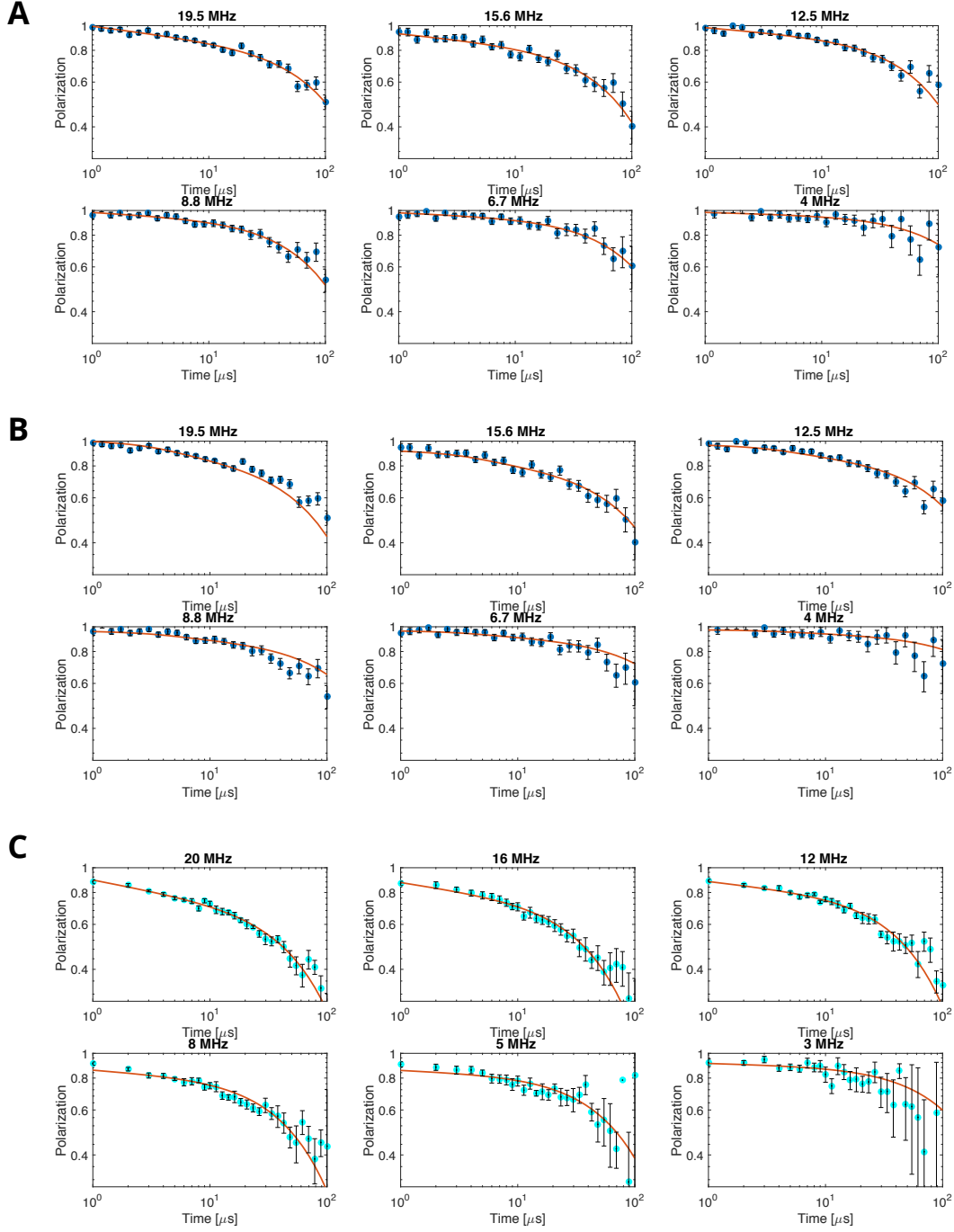


FIG. S11. **Polarization decay of a NV ensemble under Hartmann-Hahn conditions.** An initially polarized group A spin ensemble interacts with (A,B) unpolarized and (C) fully polarized group B. Solid lines are theoretical fits based upon a time-dependent disorder model with extracted parameters ( $W_d, \tau_d$ ) via a Monte-Carlo optimization. In (A,C), the spectral diffusion time  $\tau_d$  is dependent on the Rabi frequency, while in (B)  $\tau_d$  is independent of the applied Rabi frequency. The dynamical disorder strength  $W_d$  is a  $\Omega$ -independent, global variable in all three cases.

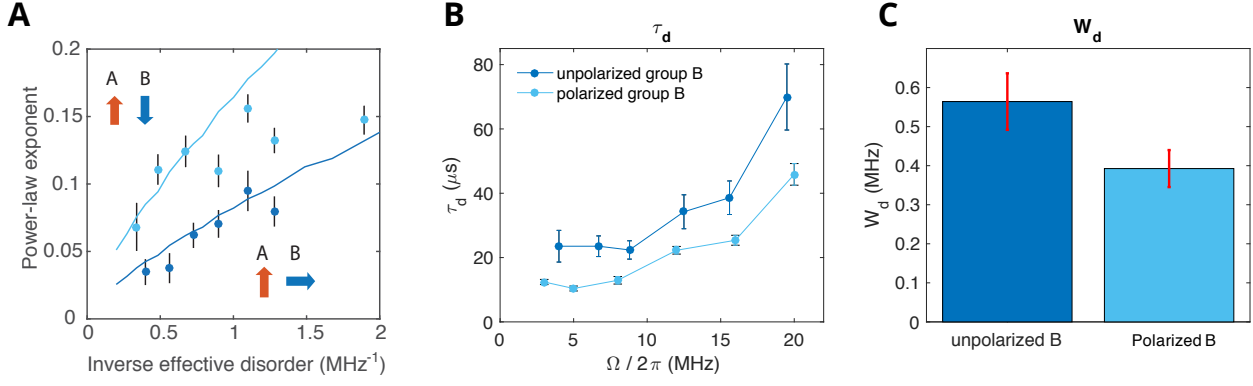


FIG. S12. **Fitted parameters of the time-dependent disorder model extracted from a Monte-Carlo optimization.** (A) Exponents of the power-law decay of group A polarization with oppositely polarized (light blue) and unpolarized (dark blue) group B as a function of inverse effective disorder. Solid lines correspond to numerical simulation results. (B) The extracted  $\tau_d$  as a function of Rabi frequency. Light and dark blue point corresponds to fully oppositely polarized and unpolarized group B spin states, respectively. (C) The extracted dynamical disorder  $W_d$ . All errorbars are evaluated from the standard deviation of the optimized parameter after running 10 independent Monte-Carlo runs.

---

\* These authors contributed equally to this work

- [1] M. J. Burek, N. P. de Leon, B. J. Shields, B. J. Hausmann, Y. Chu, Q. Quan, A. S. Zibrov, H. Park, M. D. Lukin, and M. Loncar, Nano letters **12**, 6084 (2012).
- [2] J. Choi, S. Choi, G. Kucsko, P. C. Maurer, B. J. Shields, H. Sumiya, S. Onoda, J. Isoya, E. Demler, F. Jelezko, N. Y. Yao, and M. D. Lukin, Phys. Rev. Lett. **118**, 093601 (2017).
- [3] E. Van Oort and M. Glasbeek, Chemical Physics Letters **168**, 529 (1990).